EPJ manuscript No.
(will be inserted by the editor)

Ab initio investigation in $PbZrO_3$ antiferroelectric: Structural and vibrational properties

Safari Amisi

[1] Laboratoire de Physique des Solides et des Interfaces, Institut Supérieur Pédagogique de Bukavu, Democratic Republic of the Congo.
[2] Physique Théorique des Matériaux, Université de Liège, B-4000 Sart Tilman, Belgium. e-mail: safari.amisi@uliege.be

Received: date / Revised version: date

Abstract. Using first-principles calculations, we investigate the structural and vibrational properties of $PbZrO_3$. Starting from the high-symmetry cubic perovskite phase, for which the phonon dispersion curves are reported to have many unstable branches, we identify some key intrinsic characteristics allowing the prediction of materials with the propensity of developing an antiferroelectric behavior. We confirm the key role that *R* antiferrodistortive modes play in condensing the observed antiferroelectric phase, *via* a cooperative bilinear coupling, and the nearest with the ferroelectric state. Our work shows that, given all their important potential wells none of the individual modes condensed deletes all other and that it is their coupling which plays a key role in the condensation of the ground state lead zirconate, and these couplings would explain why *Pbam* and *R*3*c* phases are close in energy for promoting the first order transition.

1 Introduction

The reason why materials become antiferroelectric remained the subject of several studies since their first discovery. The $PbZrO_3$ (PZO) is the first perovskite antiferroelectric (AFE) to be discovered [1,2] and more studied until today. The properties of this crystal are determined by the strong competition between ferroelectric and antiferroelectric ordering. In the vicinity of 230°C this compound is in the stable phase centrosymmetric orthorhombic AFE *Pbam* ($a = \sqrt{2}a_0$, $b = 2\sqrt{2}a_0$ and $c = 2a_0$) and (ii) beyond this temperature it crystallizes in the ideal perovskite cubic phase [3,4,5,6,7,8,9,10]. An intermediate phase, in a temperature range of about 5°C around 230°C was established later (230-233°C on heating and 232-227°C on cooling), although its nature and atomic structure has been much discussed [11]. On one hand, this intermediate phase was suggested as a ferroelectric (FE) rhombohedral phase *R*3*m*, experimentally in highly pure PZO samples [12,13,14] and theoretically [15,16,17,18]. The local density approximation (LDA) calculation has even demonstrated the coexistence of these both FE and AFE instabilities in PZO, with a very delicate balance between them [15,19]. On the other hand, the intermediate phase was identified as an AFE phase, named AFE-II, compared to the ground state AFE-I [11,20]. Independently, other works also announced the possibility of the presence of ferroelectricity, initially estimated to 25 μC/cm^2 [21] and to a much lower value (0.05 - 0.09 μC/cm^2) [22,23] in [001] direction in the fundamental AFE orthorhombic state, concluding non centrosymmetric space group *Pba*2 (AFE-FE) [16]. But the identification of that ferroelectric stays very hypothetical, as we will show in the following sections. The space group *Pbam* to the ground state remains the most sustained [24].

The phonons curves calculated in cubic prototype ($Pm\bar{3}m$) reveal the transitions phase that can undergoes perovskites ABO_3 compounds according to the temperature. Among all instabilities, those caused by the rotations of oxygens octahedra, antiferrodistortive (AFD) modes, are the most common in perovskites [25,26,27]. The AFD modes play a crucial role in condensing the PZO ground state, as they select the observed AFE phase, among competing structural variants, *via* a cooperative bilinear coupling [28], and at low temperature the rhombohedral *R*3*c* symmetry (AFD/FE) is energetically close to the ground state *Pbam* (AFD/AFE) [29,30]. A recent experimental result describes a detailed polarized IR and Raman spectroscopic study of AFE PZO [31]. However, a systematic and thorough theoretical study of condensation of phonon modes in PZO phases, observed or non observed, would allow better understanding the ground state in this compound. It is then the purpose of this paper to examine deeply the evolution of AFD distortion and the proximity of the FE and antipolar phases in an AFE compound like the PZO.

What is AFE phase? According to the last definition proposed by Rabe K. M. (Ref. [32]), AFE is as a FE phase in the sense that its structure is obtained by a distortion of a high symmetry nonpolar phase; for the FE phase distortion is polar, while for the AFE phase it's non-polar. However, all non-polar phases thus obtained are not AFE: there must be, in addition, an alternative low energy FE phase obtained as a distortion of the same high symmetry reference, and application of an electric field must induce a first order transition AFE−FE phase producing a double hysteresis loop characteristic. The latter condition promotes a small energy difference and ease of transformation between the two phases. Paradoxically, the study of the antiferroelectricity of PZO was often based on the understanding of the ground state. In fact, the key could be the nearest with the FE state.

In the present paper, we focus on the delicates competitions between instabilities and interactions in PZO, we analyse in details the phase transition mechanism in this system, this effects on the volume and atomics displacements. Our results show a possible coexistence of *R*3*c* and *Pbam* phases and reject the existence of *Pba*2 symmetry. Details on computational method used in our calculations are described in Section 2. The cubic structure, the phonons curves in cubic phase are analysed in Section 3, and the Section 4 analyse the *Pbam* phase. We investigate the individual antiferrodistortive, anti-polar and ferroelectric instabilities in Sections 5, 6 and 7, respectively. The combination of all these instabilities in Section 8 allow us to speculate about the low energy phase in PZO. The conclusion is given in the last Section.

2 Technical details

We performed first-principles calculations in the framework of density functional theory (DFT) thanks to the ABINIT package [33,34,35,36]. We worked within the generalized gradient approximation using the functional proposed by Wu and Cohen (GGA-WC) [37], adopting a plane-wave pseudopotential approach, with optimized pseudopotentials generated thanks to OPIUM [38]. The 6*s*, 6*p* and 5*d* levels of Pb, 4*s*, 4*p*, 4*d* and 5*s* levels of Zr and 2*s* and 2*p* levels of O were considered as valence states. Some results have been checked at the local density approximation (LDA) level using Teter's extended norm conserving pseudopotentials. Convergency was reached for an energy cutoff of 45 Ha for the plane-wave expansion and a 8×8×8 grid of *k*-points for the Brillouin zone sampling of the single perovskite cell with 5 atoms. When condensing the AFD and anti-polar (AP) instabilities, we considered on one hand a 20 atoms supercell corresponding, for *Imma* and *Pnma* phases, to $\sqrt{2}a_0$, $\sqrt{2}a_0$, $2a_0$ and a sampling of 6×6×4 *k*-points. On another hand, to relax the *Cmcm*, *R*3*c*, *Abm*2 and *Pbam* phases, we considered a 40 atoms supercell corresponding to $2a_0$, $2a_0$, $2a_0$ and a sampling of 4×4×4 *k*-points, and to $\sqrt{2}a_0$, $2\sqrt{2}a_0$, $2a_0$ and a sampling of 6×3×4 *k*-points, respectively. We explicitly checked that the relative energy of the different phases is well converged and independent of the choice of the supercell. Structural relaxations were performed until forces and stresses are smaller than 10^{-7} Ha/Bohr and 10^{-8} Ha/Bohr^3, respectively. The phonon frequencies, Born effective charges and electronic dielectric tensor were calculated according to density functional perturbation theory (DFPT) [39]. To analyse the group theory and relative contributions of different phonon modes to the distortions, we employed ISOTROPY programs [40] and AMPLIMODES code of Crystallographic Bilbao server [41,42].

3 Cubic perovskite structure

In the high symmetry cubic phase of perovskite structure, the atomic positions are fixed by symmetry, and the only structural parameter to be relaxed is the lattice constant *a*. The result of calculation is reported in table 1 and compared with other theoretical and experimental values. Our relaxed lattice constant $a_0 = 4.138$ Å is in good agreement with the experimental data, with only a discrepancy of 0.2%. As expected, the LDA tendency is to underestimate the lattice constant, while the GGA-PBE tends to over-estimate more than the GGA-WC. As we shall see later in the analysis of the ground state, the competitions between various instabilities in the PZO are very sensitive to these trends functional.

Approach	Method	a_0	Ref.
Experiment	X-rays	4.13 (0 K)	[43,44]
		4.1614	[45]
Theory	PW-PP (GGA-WC)	4.138	Present
	PW-PP (LDA)	4.102	Present
	PW-PP (LDA)	4.12	[15]
	FLAPW (GGA-PBE)	4.18	[17]
	B3LYP	4.220	[46]

Table 1. Cubic lattice parameters (Å) of PZO compound, obtained by different and various functional methods compared to experimental data. The experimental value 4.13 Å (Ref. [44]) was extrapolated to 0 K.

Our calculations describe the PZO as a good insulator with a direct band gap 2.33 eV at *X* point, almost equal to the indirect band gap between *R* and *X* points of the Brillouin zone. The feature of the GGA is, among others, to underestimates from about 30 to 40%, the experimental band gap, which is 3.70 eV [47] but correctly reproduces the insulating nature of this compound. The B3LYP exchange-correlation functional overestimates the gap for this compound (5.63 eV) [46].

Even if the ground state of a system can be more complex, the calculation of phonon dispersion curves in the high symmetry cubic phase (5-atoms) offers a global view of the instabilities that can progressively condense, to give the possible intermediate

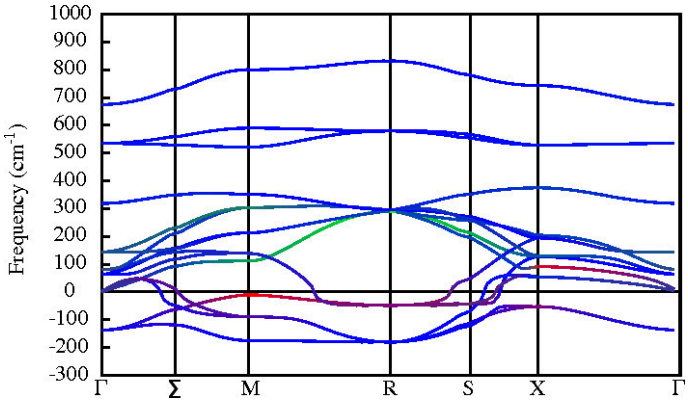

Fig. 1. (Color online) Calculated phonon dispersion curves of cubic PZO at the GGA-WC volume along the path $\Gamma-\Sigma-M-R-S-X-\Gamma$ of the cubic Brillouin zone. A color has been assigned to each point based on the contribution of each kind of atom to the associated dynamical matrix eigenvector (red for the Pb atom, green for the Zr atom, and blue for O atoms).

phases and the ground state. In Fig. 1 we report the phonon dispersion curves of PZO cubic. The lines $\Gamma-M$ (going through the Σ point), $M-R$, $R-X$ (going through the S point), and $X-\Gamma$ are along [110], [001], [011] and [100] directions, respectively. Negative values of ω (cm^{-1}) in the graphs correspond to imaginary phonon frequencies and are related to unstable modes, which determine the nature of eventually phase transitions. The character of these modes thus also has significant implications on system properties.

Frequencies and types ferroic unstable modes are summarized in table 2.

k-points		Mode	Type	ω	
				GGA-WC	LDA
Γ	(0, 0, 0)	Γ_4^-	(FE)	137i	143i
X	$(\frac{1}{2}, 0, 0)$	X_5^+	(AP)	52i	58i
M	$(\frac{1}{2}, \frac{1}{2}, 0)$	M_3^+	(AFD)	175i	190i
		M_5^-	(AP)	89i	100i
		M_2^-	(AP)	10i	16i
R	$(\frac{1}{2}, \frac{1}{2}, \frac{1}{2})$	R_4^+	(AFD)	180i	196i
		R_5^+	(AP)	48i	53i
Σ	$(\frac{1}{4}, \frac{1}{4}, 0)$	Σ_2	(AP)	121i	
		Σ_2	(AP)	62i	
S	$(\frac{1}{2}, \frac{1}{4}, \frac{1}{4})$	S_4	(AFD/AP)	128i	
		S_4	(AFD/AP)	50i	

Table 2. Modes and soft phonon frequencies ω (cm^{-1}) of PZO cubic at Γ, X, M, R, Σ and S points of the Brillouin zone.

As shown in the table 2, the GGA-WC and LDA functional shows the same trend between different instabilities, although the LDA accentuates AFD modes. The Fig. 1 shows the existence of many unstable modes branches. Γ_4^-, Σ_2, X_5^+, M_5^- and R_5^+ unstable modes are dominated by the movement of Pb and O atoms with a small contribution of Zr atom, modes corresponding to the movement of Zr against O being all become stable. While in the $PbTiO_3$, instabilities are dominated by Γ_4^- mode, in $PbZrO_3$ the AFD (M_3^+ and R_4^+) and AP (Σ_2, X_5^+, M_5^- and M_2^-) instabilities are also considerable. For the instability at Γ point, the eigendisplacement is significantly dominated by the movement in opposite directions of Pb and O atoms, while contrary to what is observed in the ferroelectric perovskites, the Zr now appears to move not *against* but *with* the oxygens. The S_4 distortion is a bit complex: it has a mixed character, combining AFE features with others that are reminiscent of AFD modes. We will call for that AFD/AP mode. The AFD/AFE centrosymmetric phase *Pbam*, as we shall see in the next section, is obtained by condensing the main modes AFD at R and AP at Σ (Fig. 1) in the cubic plane [110].

4 The Pbam phase

According to the literature, the *Pbam* AFD/AFE centrosymmetric orthorhombic phase is the ground state of $PbZrO_3$. Let's start by talking about the *Pba*2 alternative noncentrosymmetric phase that is supposed to add ferroelectricity to *Pbam* group in z direction, perpendicular to the [110] plane (R_4^+, Σ_2 and Γ_4^- modes) [21]. We calculated the energy gains from the high symmetry relative phase as well as the phonons in these relaxed phases, and compared the calculated to experimental phases with a mode by mode decomposition. Our calculations showed that, regardless of the used functional (GGA-WC or LDA), starting from the alternative *Pba*2 experimental phase the system always relaxes in *Pbam* phase. The PZO compound therefore preferred centrosymmetric *Pbam* phase in place of the noncentrosymmetric *Pba*2 phase. This is confirmed by the fact that the phonon calculations of *Pbam* phase show no instability. This result allows us to affirm that, contrary to what is suggested by some experiments [21], the appearance of an additional ferroelectricity in *Pbam* phase is unlikely. In table 4 we present the structural parameters and atomic positions of PZO in *Pbam* orthorhombic phase and compare with other theoretical and experimental data.

	Présent			Expt. (10 K)[48]			LDA[49]			GGA-PBE[17]		
V	70.60											
a	5.8740			5.8736			5.8752			5.9636		
b	11.7650			11.7770			11.7742			11.7724		
c	8.1719			8.1909			8.2077			8.3428		
Site	x	y	z	x	y	z	x	y	z	x	y	z
Pb1(4g)	0.7011	0.1239	0.0000	0.6991	0.1228	0.0000	0.6948	0.1233	0.0000	0.6933	0.1226	0.0000
Pb2(4h)	0.7109	0.1284	0.5000	0.7056	0.1294	0.5000	0.7009	0.1300	0.5000	0.7059	0.1291	0.5000
Zr1(8i)	0.2410	0.1242	0.2497	0.2414	0.1248	0.2404	0.2404	0.1240	0.2493	0.2412	0.1244	0.2493
O1(4g)	0.2752	0.1567	0.0000	0.2756	0.1560	0.0000	0.2789	0.1570	0.0000	0.2750	0.1526	0.0000
O1′(4g)	0.2988	0.0949	0.5000	0.3011	0.0956	0.5000	0.2989	0.0956	0.5000	0.2997	0.0954	0.5000
O2(8i)	0.0318	0.2613	0.2804	0.0317	0.2622	0.2798	0.0324	0.2615	0.2812	0.0314	0.2620	0.2794
O3(4f)	0.0000	0.5000	0.2041	0.0000	0.5000	0.2056	0.0000	0.5000	0.2033	0.0000	0.5000	0.2029
O4(4e)	0.0000	0.0000	0.2295	0.0000	0.0000	0.2293	0.0000	0.0000	0.2268	0.0000	0.0000	0.2291

Table 3. Volume (Å^3/f.u.), relaxed and experimental lattice parameters (Å) and atomic positions in the PZO *Pbam* orthorhombic. The reference LDA relaxation was made with experimental lattice parameters at 200 K.

The *Pbam* orthorhombic lattice parameters (Table 4) are related to the pseudo-cubic lattice parameter $a_p = 4.1535$ Å, $b_p = 4.1699$ Å, and $c_p = 4.0860$ Å by $a = 2a_p\cos(\beta/2)$, $b = 4b_p\sin(\beta/2)$ and $c = 2c_p$, where the angle $\beta = 90°$. At low temperature c_p is smaller than a_p and b_p and increases rapidly with temperature. Therefore, every lattice pseudo-cubic parameters converge at high temperatures. One possible explanation for this behavior would be in terms of the rotation of the BO_6 octahedron. An important consequence of rotations is to reduce the lattice parameters in the directions perpendicular to the axis about which turns the octahedron [20,26]. And it is the combination of rotations around the [100] and [010] directions which produces [110] rotation observed in the PZO AFE phase, reducing the length c of the cell.

Let's now give a more quantitative analysis of modes contributing to the development of *Pbam* phase. In Fig. 2, we present the amplitudes of the phonon modes which condense in this phase relaxed in GGA-WC (red columns) and LDA (blue columns) and we compare them with the experimental phases (dark green columns).

Fig. 2 show that we have a total of six modes, including two major (AFD R_4^+, and AP Σ_2) and four additional (S_4, R_5^+, X_3^-, and M_5^-) which condense in the *Pbam* AFD/AFE phase of PZO. Looking first at the breakdowns of the modes R_4^+ is the mode that seems to dominate, followed by Σ_2 mode and other additional modes. The result obtained is consistent with the findings of Refs. [29,50,51] who attributed the *Pbam* status for PZO to this high AFD instability at R point. The table 4 shows the relative contributions of each six irreducible representation to the *Pbam* distortion, according to the analysis made by the AMPLIMODES code compared to the experimental observations [52,20]. For the two main modes, their contributions are reversed according to the calculated and the experimental observed contributions (Table 4). This could be explained by the fact that, in AMPLIMODES [41,42] the analysis consists in decomposing the symmetry-breaking distortion present in the distorted structure into contributions from different symmetry-adapted modes, whereas the experimental observations would use other parameters such as eigendisplacements for example taking into account the atom masses.

In Ref. [11], it was demonstrated that *Pbam* phase transition in PZO can be considered as a sequence of the transitions related first to the condensation of R-component and then to that of the Σ-component. It is the Σ_2 mode, as we will see in the

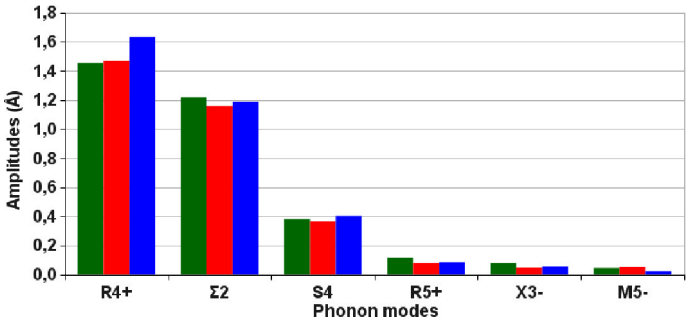

Fig. 2. (Color online) Relative contributions of phonon modes, according to the AMPLIMODES code, in the *Pbam* phase of PZO relaxed in GGA-WC (red columns) and LDA (blue columns) compared to the experimental data (dark green columns, Ref. [48]).

	R_4^+	Σ_2	S_4	R_5^+	X_3^-	M_5^-
Present	0.463	0.366	0.115	0.025	0.015	0.017
Expt. [52,20]	0.301	0.664	0.017	0.012	0.002	0.004

Table 4. The relative contributions of each irreducible representation to the *Pbam* distortion of PZO made by the AMPLIMODE code compared to the experimental observations.

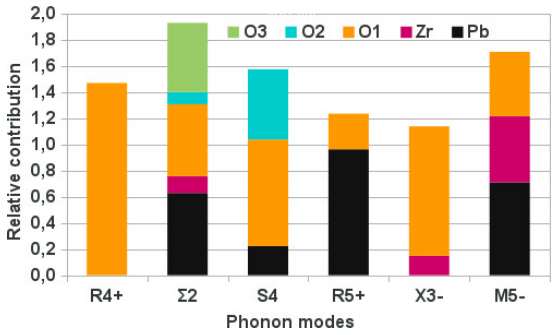

Fig. 3. (Color online) Atomic contributions by mode in the *Pbam* phase of PZO.

Section 6, which yield the AFE cation displacement pattern in PZO. Rotation mode R_4^+ does not attribute the symmetry group but prepares it by doubling along the z axis. In this structure, the additional modes S_4, R_5^+, X_3^- and M_5^- appear without breaking of additional symmetry. It is instructive to compare the contribution of each atom to the distortion associated with each irreducible representation (Fig. 3).

Analyzing the individual contributions of atomic displacements, it appears that in the M_5^- mode, unlike the GGA-WC calculation shown in Fig. 3, the LDA calculation rather promotes oxygen instead of Pb (Expt./GGA-WC/LDA, Pb = 0.036/0.038/0.004 and O = 0.026/0.026 /0.022), as well as in the Σ_2 mode (Expt./GGA-WC /LDA, Pb = 0.789/0.728/ 0.642 and O = 0.657/0.636 /0.727). We note the agreement between the GGA-WC values and the experimental data.

Let's now in the next three sections, look to condensation individual modes AFD, AP and FE to understand their evolution in the stabilization of the state of lower energy in PZO.

5 Antiferrodistortive instabilities

The AFD R_4^+ and M_3^+ modes were observed in the phonon dispersion curves in the PZO paraelectric (PE) cubic phase, with more larger amplitudes imaginary frequencies ($180i$ cm^{-1} and $175i$ cm^{-1}, respectively, Table 2) than FE polar and AP modes (Γ_4^-, $137i$ cm^{-1}; S_4, $128i$ cm^{-1}; Σ_2, $121i$ cm^{-1}). So, what phase stabilizes the PZO it was only AFD? The AFD modes typically have, in fact, the lowest energy at R and M points of the Brillouin zone. In Fig. 4, we report for the AFD phases, energy gain, the rotation angles of the oxygen octahedra and the volume, calculated with two functional, GGA-WC and LDA, compared to the high symmetry cubic phase.

Depending on the energy gain obtained in each of the AFD phases shown (Fig. 4) we see that, regardless of the functional used purely AFD state lowest energy in the PZO is in the orthorhombic phase *Pnma* ($a^-b^+a^-$). This phase is not observed in this material. Let's look to the individual modes M_3^+ and R_4^+. Relaxation of AFD mode in phase (M_3^+) is more favorable when

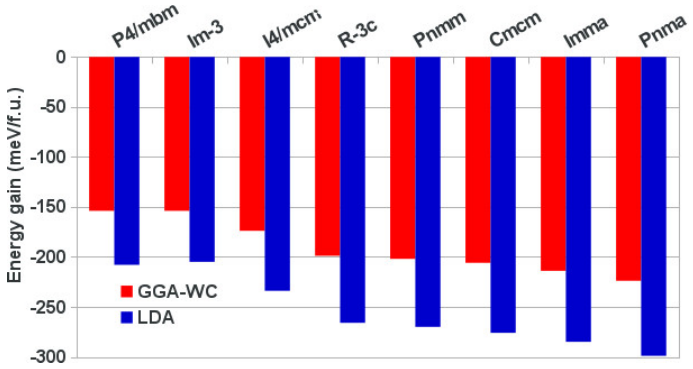

Fig. 4. (Color online) Energy gain ΔE (meV/f.u.) relative to the PE phase in AFD related phases in PZO. Amplitudes of AFD rotation angles (°) and volume (Å^3/f.u.) are respectively: *P4/mbm* ($a^0a^0c^+$: $c^+ = 11.5$, V = 69.73), *Im*$\bar{3}$ ($a^+a^+a^+$: $a^+ = 6.4$, V = 69.99), *I4/mcm* ($a^0a^0c^-$: $c^- = 11.9$, V = 69.64), *R*$\bar{3}c$ ($a^-a^-a^-$: $a^- = 7.0$, V = 69.74), *Pnmm* ($a^-b^+b^+$: $a^- = 9.4$, $b^+ = 7.8$, V = 69.76), *Cmcm* ($a^0b^-c^+$: $b^- = 9.2$, $c^+ = 8.7$), *Imma* ($a^-a^-c^0$: $a^- = 9$, V = 69.71), *Pnma* ($a^-b^+a^-$: $a^- = 7.8$, $b^+ = 7.4$, V = 69.58).

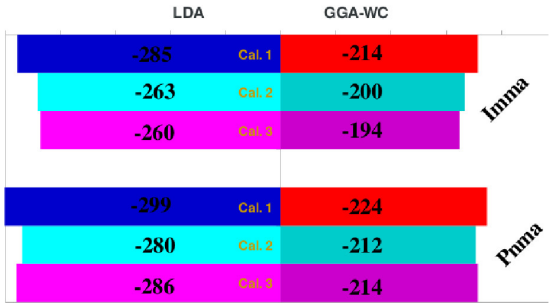

Fig. 5. (Color on line) Energy gains (meV/f.u.) of *Imma* and *Pnma* phases in the relaxed PZO compared to the cubic phase. The energies were calculated with two functional, GGA-WC and LDA, and consist of three calculations, as described in the text.

condensed around a single direction ($a^0a^0c^+$, *P4/mbm*) than in three directions ($a^+a^+a^+$, *Im*$\bar{3}$) with equal energy in GGA-WC for both symmetries (-154 meV/f.u.) and a slight decrease in favor of *P4/mbm* phase in LDA calculation. From the results of our calculations, the AFD mode in antiphase (R_4^+) it's more favored when condensed simultaneously on two directions. The *Imma* phase ($a^-a^-c^0$, -214 meV/f.u.) is in fact lower in energy than the phases *I4/mcm* ($a^0a^0c^-$, -174 meV/f.u.), antiphase rotation around a single direction and *R*$\bar{3}c$ ($a^-a^-a^-$, -199 meV/f.u.), antiphase rotation around three directions. By comparing the energy gains of the two separate modes, we note that the AFD instability phase (M_3^+) is energetically disadvantaged compared to AFD instability in antiphase (R_4^+) in PZO. It is the same with the amplitudes of octahedral rotations.

To analyse the effect of the strain and cation displacement on energy gain for *Imma* and *Pnma* phases, we did three calculations in GGA-WC and LDA (Fig. 5): The first calculation, we'll call the current calculation (cal. 1), was to allow the relaxation of the strain, i.e. by making a complete relaxation lattice parameters and atomic positions, in the second calculation (cal. 2), we were relaxing only atomic positions in the cubic volume (cubic lattice parameter fixed), i.e. by not allowing the strain to relax, and the third type of calculation (cal. 3), meanwhile, was to also relax the lattice parameters and atomic positions, as for the calculation (cal. 1), but by setting the cations to their high symmetry positions.

If we compare the energy gains of calculations (cal. 1) and (cal. 3), we find that the *Imma* phase has a lower energy in complete relaxation (cal. 1) than the *R*$\bar{3}c$ phase (-214 meV/f.u. < -199 meV/f.u.), but when we set the cations to their high symmetry positions (cal. 3), the first becomes disadvantaged in favor of the second (-194 meV/f.u. > -199 meV/f.u.). Such as shown in Fig. 6, unlike *I4/mcm* and *R*$\bar{3}c$ phases that only allow the rotations of oxygen (R_4^+ mode), the *Imma* phase allows additional AP displacement Pb cations (R_5^+ mode), and it is this coupling which makes stable the *Imma* phase than *R*$\bar{3}c$. Singh [19] reported the LDA-LAPW energies of pure rotations *I4/mcm*, *Imma* and *R*$\bar{3}c$ in PZO fixing cations and effectively identified, in agreement with our calculations, the *R*$\bar{3}c$ phase as the most stable (-188 meV/f.u., -223 meV/f.u. and -234 meV/f.u., respectively). But while its angles calculated rotations appear to change in any way (*I4/mcm*, 11.9°; *Imma*, 12.7°; and *R*$\bar{3}c$, 10.4°) our calculated angles decrease when the oxygens turn around [100], [110] and [111] directions, respectively (*I4/mcm*, 11.9°; *Imma*, 8.6°; and *R*$\bar{3}c$, 7.0°).

Now combining the two modes of rotation M_3^+ and R_4^+, we note in agreement with the analysis of the preceding individual condensations, the unfavorable nature of the condensing inphase rotations (M_3^+) in two directions, with the *Pnmm* phase ($a^-b^+b^+$, -202 meV/f.u.) slightly higher in energy than the *Cmcm* phase ($a^0b^-c^+$, -206 meV/f.u.). The *Pnma* phase ($a^-b^+a^-$), combining two antiphase rotations (R_4^+) and one inphase rotation (M_3^+) reveal to be the lowest energy phase of all. Coupling of these two

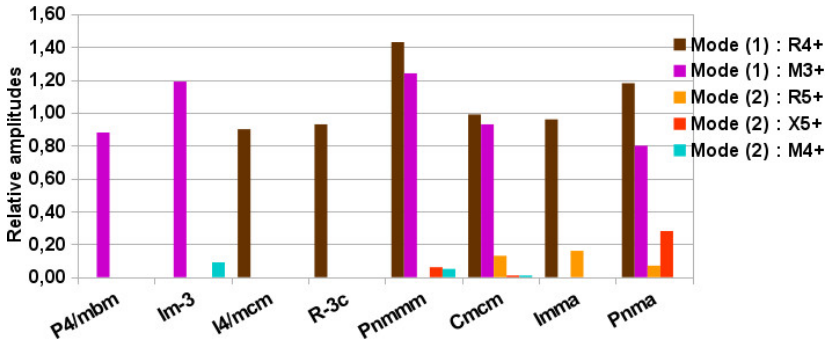

Fig. 6. (Color on line) Relative amplitudes of modes contributing to the condensation of several AFD distortions relaxed in PZO. The main modes (1) consist of octahedra rotation of oxygens and additional modes (2) consist of couplings with cations (R_5^+ and X_5^+) or displacement of oxygen (M_4^+). Pb contribution is greater than that of oxygen in the R_5^+ mode, while the opposite is true in the X_5^+ mode.

rotations modes has the effect including reducing their amplitudes octahedral rotations. An important question is why it is rather the $a^-a^-c^0$ distortion of *Imma* AFD phase contributes to the onset of *Pbam* AFD/AFE phase, as we saw in the Section 4, rather than the $a^-b^+a^-$ distortion of *Pnma* phase which is energetically more favorable it.

On the basis of Fig. 5, we first note that even in the absence of coupling with the cation movements (cal. 3), the *Pnma* phase is the most favorable combination of rotations. In Fig. 6 we summarize the relative amplitudes of modes which condense in the AFD phases of PZO.

Analyzing the Fig. 6, we see that, in agreement with Ref. [29] some AFD modes combinations allow the emergence of additional cationic relaxations through trilinear couplings with AP modes type $\lambda Q_{M_3^+} Q_{R_4^+} Q_{X_5^+}$ or $\lambda Q_{M_3^+} Q_{R_4^+} Q_{R_5^+}$. This is the case of *Cmcm* ($a^0b^+c^-$), *Pnmm* ($a^-b^+b^+$), less favored here, and *Pnma* ($a^-b^+a^-$) phases. In the *Imma* ($a^-a^-c^0$) phase, with $\lambda = 0$ so it become a bilinear coupling [28], the coupling is done with the R_5^+ mode (Fig. 6) and allow substantial additional energy gain (20 meV/f.u., Fig. 5) bringing this phase at the *Pnma* energy state. In the latter, coupling with the R_5^+ mode is also allowed, but it is a coupling with the X_5^+ mode which becomes dominant and stabilizes this phase through additional energy gain of 10 meV/f.u. The X_5^+ mode stabilizing *Pnma* phase consist of an AP distortion of Pb cations, with a greater contribution of the oxygen in the *ab* orthorhombic plane, i.e. in the cubic [100] direction, while R_5^+ mode stabilizing the *Imma* phase also consist of an AP displacement of Pb cations, and with a greater contribution of Pb, but in the orthorhombic *a* direction, i.e. in the cubic [110] direction. However, the Σ_2 AP mode, as described in the next section, condensing into *Pbam* AFD/AFE phase is also in the cubic [110] direction. This may explain why coupling the Σ_2 distortion of AP *Pbam−II* phase with $a^-a^-c^0$ of the *Imma* phase is more favored in the condensation of AFD/AFE *Pbam* more than with the *Pnma* ($a^-b^+a^-$) phase. In table 5, we characterize the *Imma* phase in the PZO and the unstable modes which are observed by our calculations.

Mode	R_4^+ (*Imma*)					
	Present			Ref. [53]		
Site	*x*	*y*	*z*	*x*	*y*	*z*
Pb (4e)	0.0000	0.2500	0.2334	0.0000	0.2500	0.2564
Zr (4d)	0.2500	0.2500	0.7500	0.2500	0.2500	0.7500
O1 (8f)	0.2054	0.0000	0.0000	0.28175	0.0000	0.0000
O3 (4e)	0.0000	0.2500	0.6744	0.0000	0.2500	0.809
U-modes	Σ_2 (62*i*), M_3^+ (53*i*), M_5^- (41*i*)					

Table 5. Volume (69.71 Å^3/f.u.) and lattice parameters ($a = 8.157$ Å, $b = 5.824$ Å, $c = 5.870$ Å) of AFD *Imma* orthorhombic structure relaxed in PZO. We report the atomic positions, the frequencies of imaginary phonons (cm^{-1}) and their relative unstable modes (U-modes).

The results of table 5 comforts us in our analysis: *Imma* ($a^-a^-c^0$) phase shows an AP unstable mode Σ_2 (62*i* cm^{-1}), condensing into AFD/AFE *Pbam* phase, while the *Pnma* ($a^-b^+a^-$) symmetry was deleted it (showing only M_5^- 17*i* mode). For all these reasons mentioned above we understand better why, although both AFD phases are not observed in the PZO compound, it is rather the *Imma* phase and not *Pnma*, which condenses in the *Pbam* phase favorable to AP mode in the [110] plane increasing the volume (Tables 5 and 6).

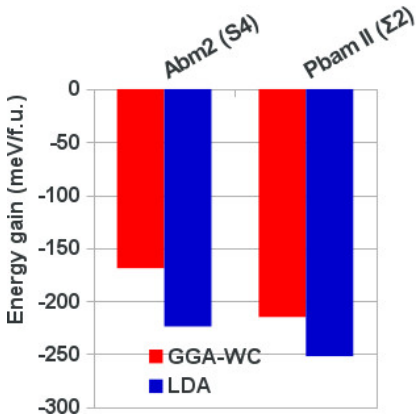

Fig. 7. (Color on line) Energy gain ΔE (meV/f.u.) compared to the parent PE phase of AFE *Abm*2 and *Pbam* 20-atoms orthorhombic structures relaxed in PZO.

6 Anti-polar instabilities

How to involve the PZO if it were only subject to AP instabilities? In their study by pulsed neutron scattering, Teslic and Egami [20] were proposed independently, instead of *R*3*m* FE phase, an intermediate phase rather AFE they named AFE-II, which result from the condensation of AP Σ_2 mode. Σ_2 mode comprises an AP displacement of Pb in the [110] plane causing a multiplication cell size of the factors $\sqrt{2}$ and $2\sqrt{2}$, respectively. We also condense the AFD/AP S_4 mode. In Fig. 7 we report the energy gains of *Abm*2 and *Pbam* 20-atoms subgroups obtained by condensing and relaxing unstable modes AP at Σ, Σ_2 mode, and S, S_4 mode, k-points respectively.

Mode	Σ_2 (*Pbam*)					
	Present			Ref. [53]		
Site	x	y	z	x	y	z
Pb (4g)	0.6946	0.1444	0.0000	0.70285	0.625	0
Zr (4h)	0.2415	0.1186	0.5000	0.7583	0.375	0.5
O1 (4g)	0.2841	0.1418	0.0000			
O2 (4h)	0.0401	0.2619	0.5000	0.536	0.7379	0.5
O3 (2d)	0.0000	0.5000	0.5000	0.0000	0.5000	0.5
O4 (2b)	0.0000	0.0000	0.5000	0.0000	0.0000	0.5
U-modes	$S_3+X_4^-+R_4^++R_5^+$ (68i)					
	$R_4^++S_4+R_5^++X_3^-$ (47i)					
	$\Gamma_4^-+\Sigma_4+M_5^+$ (37i)					

Table 6. Volume (72.03 Å^3/f.u.) and lattice parameters (a = 5.961 Å, b = 11.780 Å, c = 4.103 Å) of AFE *Pbam* 20-atoms orthorhombic structure relaxed in PZO. We report the atomic positions, the frequencies of imaginary phonons (cm^{-1}) and their relative unstable modes (U-modes).

By observing the energy gains of these two AP phases (Fig. 7), we find that the AP state lowest energy in the PZO is *Pbam* phase containing 20 atoms. This *Pbam* 20-atoms hypothetical structure, condensed from eigenvectors associated Σ_2 mode proved to be, after relaxation, a sum of Σ_2 AP, senior and M_5^-, additional, modes. We then found it useful to only report in table 6 the lattice parameters and the remaining unstable modes in the *Pbam* subgroup (AP) 20-atoms, as is it contribution that is the most important to condense the *Pbam* phase (AFD/AFE) 40-atoms.

The calculation of phonon frequencies in the AP phase *Pbam* 20-atoms, having unstable modes observed, shows that, unlike the $BaTiO_3$ and $PbTiO_3$ compounds couplings between different modes play a considerable role in the condensation of instabilities in the PZO. The eigendisplacement associated to only AP Σ_2 mode already give the *Pbam* space group, thus the AFD R_4^+ mode does not assign the space group, but only contribute by doubling the cell along the c axis perpendicular to AFE plane and lower energy. To differentiate it from the *Pbam* phase (AFD/AFE), we will call *Pbam*$-II$ this phase purely AFE in the following. The coexistence of AFD and AFE phases nearly energy (*Imma*, -214, and *Pbam*$-II$, -215, respectively) emphas that the *Pbam*

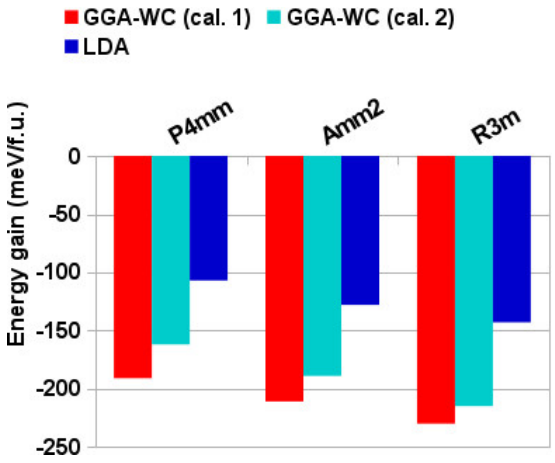

Fig. 8. (Color on line) Energy gain ΔE (meV/f.u.) compared to the parent PE (V = 70.85 Å^3/f.u.) phase for FE phases with polarization along [001] (FE$_z$: 74.6 μC/cm^2), [110] (FE$_{xy}$: 72.7 μC/cm^2) and [111] (FE$_{xyz}$: 75 μC/cm^2, V = 72.34 Å^3/f.u.) relaxed in PZO. The energies were calculated with two functional, GGA-WC (cal. 1 and cal. 2) and LDA as previously explained.

phase transition is triggered by a bilinear coupling that drives simultaneously AP displacements and octahedral tilts [28]. Let's finally identify the purely FE phase lowest energy in the PZO.

7 Ferroelectric instability

In the phonon dispersion curves of the cubic phase (Fig. 1), we have identified a not insignificant FE instability at the zone center (Γ_4^-, 137i cm^{-1}). After analyzing the individual condensations AFD and AP modes in the PZO and have identified the *Pnma* and *Pbam−II* structures as purely AFD and AP states lowest energy, respectively, let's now characterize the FE instability observed in the high symmetry parent phase of PZO in order to identify purely FE phase lower energy.

As observed in $SrZrO_3$ [54], in the cubic phase, the eigendisplacement vector of the Γ polar instability in PZO is dominated by opposite displacements of Pb and O atoms, while the Zr atoms move in the same direction as the O atoms but with a much smaller amplitude. In the cubic symmetry, FE unstable mode is three times degenerate. We then compared the energies of phases with the polarization along three different directions in order to identify the FE polar phase lowest energy: FE$_z$ (*P*4*mm*) phase with a polarization oriented in the [100] direction, FE$_{xy}$ (*Amm*2) phase with a polarization oriented in [110] direction and FE$_{xyz}$ (*R*3*m*) with a polarization along the diagonal [111]. We present in Fig. 8 energy gains from the cubic phase high symmetry of the three FE polar phases related in PZO, respectively.

Looking at the effect of strain on polar modes FE and non-polar AFD, comparing the energy calculations with relaxation of strain (cal. 1) and without relaxation of it (cal. 2), we see more strain coupling with the FE mode (gain of about 30 meV/f.u., Fig. 8) than with AFD modes (gain of about 14 meV/f.u. Fig. 5). Also, the energy gain of the AP phase *Pbam-II* (Fig. 7) is equal to the FE phase *R*3*m* (−215 meV/f.u.), when not relaxing the strain in the latter (cal. 2, Fig. 8). The observation of the volume and energy gains of AFD, AP and FE phases shows us, in fact, that the last instabilities tend to increase the volumes of cell, and are therefore favored by GGA, while rotations reduce volume of the material and are favored by the LDA method. We can express this in the relation:

$$V_{\mathrm{FE}} > V_{\mathrm{AFE}} > V_{\mathrm{PE}} > V_{\mathrm{AFD}} \tag{1}$$

This opposite evolution of FE and AFD instabilities to the volume, and therefore pressure, is a known characteristic of these two types of instabilities [22,55]. As typically observed in the family of ABO_3 compounds, FE distortions tend to increase the lattice parameter in the direction of polarization and reduce in directions perpendicular to it. The amplitudes of the spontaneous polarization in all three phases FE of PZO (75, 73 and 75 μC/cm^2, respectively) are more twice higher than those of $BaTiO_3$ (27, 30 and 33 μC/cm^2, respectively, Ref. [54]) and amplitude comparable to that of tetragonal $PbTiO_3$ (75 μC/cm^2, 295 K; Ref. [50] and it's references). The polarization value is almost the same in *P*4*mm* and *R*3*m* phases. Furthermore, by comparing, for each phase, the calculated energy of the current relaxation, i.e. with relaxation of the strain (cal. 1), and that calculated in cubic volume, i.e. without relaxation the strain (cal. 2), we find that the tetragonal and orthorhombic phases have the highest couplings with the strain, with energy gains 29 and 21 meV/f.u., respectively. The energy gain observed in three phases relaxed show that, irrespective of the functional used purely FE state of lowest energy in the PZO is rhombohedral *R*3*m*, consistent with the extrapolation of King-Smith *et al.* [43]. As it's observed in all ABO_3 compounds, all purely FE phases, the lowest energy phase also has the largest volume cell. Note another feature of PZO, for all perovskites compounds, this system with $\Delta E = -$ 230 meV/f.u., has a FE phase with the largest energy gain. For comparison, energy gains obtained by our calculations, low symmetry FE phases of the $BaTiO_3$ and $KNbO_3$ orthorhombic, $PbTiO_3$ and $SrZrO_3$ tetragonal [54] worth −23, −84, −45 and

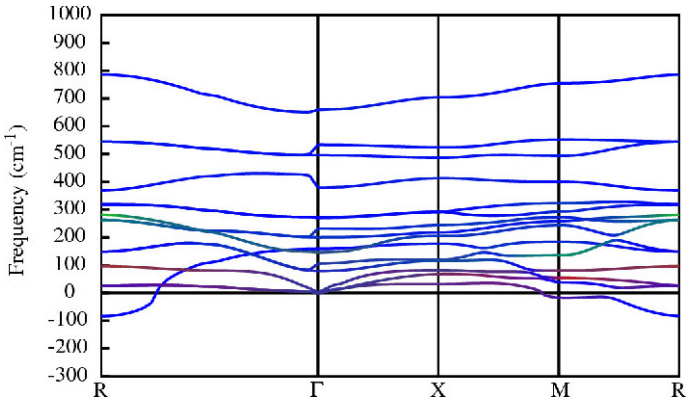

Fig. 9. (Color online) Phonon dispersion curves in the rhombohedral FE of PZO at GGA-WC volume along the path $R-\Gamma-X-M-R$ of the cubic Brillouin zone.

-30 meV/f.u., respectively. To characterize the low-energy state purely FE $R3m$ in PZO, we report the atomic displacements (Table 7), comparing them to available data, and the phonon dispersion curves (Fig. 9), all calculated in this phase to lattice parameters relaxed.

	Present		Ref.[15]	Ref.[18]
Method	GGA-WC	LDA	LDA-FLAPW	GGA-PBE
$a=b=c$	4.167	4.127	4.12	4.176
δ_{Zr}	-0.0484	-0.0489	-0.0448	-0.446
δ_{O_1}	-0.0657	-0.0649	-0.0605	-0.014
δ_{O_2}	-0.0905	-0.0935	-0.0904	-0.041
Angle (°)	89.4	89.5	-	-
U-modes	M_5^- (18i), R_4^+ (84i)			

Table 7. Lattice parameters (Å), atomic displacements and frequencies of unstable phonons (cm^{-1}) in the FE stable state rhombohedral $R3m$ of $PbZrO_3$.

Our data on atomic displacements in the rhombohedral FE are in agreement with Ref. [15], but not with the Ref. [18] (Table 7). The analysis of the atomic displacement in $R3m$ phase of PZO confirms that Γ_4^- mode is heavily dominated by displacement in opposite directions Pb and O atoms with very low contribution of Zr atom, which illustrates the importance of Pb$-$O interactions (in addition to the Pb lone-pair 6s-p electrons effect [56]) in this system. The phonon dispersion curves (Fig. 9) shows that only condensing Γ_4^- mode in the FE phase lowest energy $R3m$ in PZO also stabilizes many instabilities without deleting them all. M_5^- (AP, 18i) and R_4^+ (AFD, 84i) remain unstable.

The $R3m$ phase is the first transition, PE-FE, which passes the PZO when decrease its temperature [15,16,17,18]. By comparing the amplitudes of the frequencies of imaginary phonons in both Fig. 1 and Fig. 9, we can realize the importance of couplings between the different instabilities observed in the cubic phase high symmetry, especially between polar and AP modes.

If we compare the energy gains LDA and GGA calculations in the study of instabilities purely FE and those relating to non-polar distortions (Figs. 8, 7 and 4) we note that the LDA calculation underestimates the energy of polar distortions (FE) and is more favorable to the AP and non-polar distortions, whereas the GGA method shows but otherwise not as pronounced trend. This difference is characteristic for these two types of functional. While GGA puts all these distortions in an energy range of about 50 meV/f.u., placing the $R3m$ state purely FE lowest energy slightly lower than purely AFD lowest energy state $Pnma$ and purely AP lowest energy state $Pbam{-}II$ (FE, -230 meV/f.u. against AFD, -224 meV/f.u. and AP, -215 meV/f.u.). The GGA-WC calculation is in the middle between LDA, very favorable to the non-polar modes and GGA-PBE, very favorable to polar modes; which puts this functional in a relatively good position to characterize the material.

In summary, at this level of analysis, comparing energy gains GGA-WC, we note that it is the solitary polar mode Γ_4^- that condenses in the phase of lower energy FE rhombohedral $R3m$ ($a_+^0a_+^0a_+^0$), followed by the coupling of the non-polar modes R_4^+ and M_3^+ condensing in the AFD $Pnma$ ($a^-b^+a^-$) orthorhombic and above, by the way condensing Σ_2 mode in AP $Pbam{-}II$ phase (FE, -230 meV/f.u.; AFD, -224 meV/f.u. and AP, -215 meV/f.u.). The AFD $Imma$ phase, also orthorhombic and condensing only antiphase rotations (R_4^+) has an energy almost equal to that of the AP $Pbam{-}II$ phase (-214 meV/f.u.). Our LDA

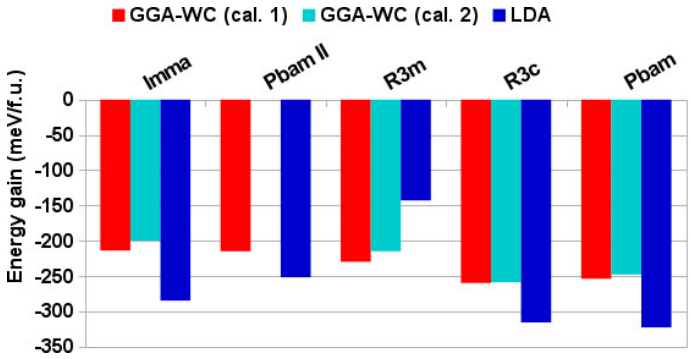

Fig. 10. (Color online) The energy gain ΔE (meV/f.u.) compared to the PE high symmetry phase of AFD *Imma* ($a^-a^-a^0$) orthorhombic, AP *Pbam-II* orthorhombic, FE *R*3*m* ($a^0_+a^0_+a^0_+$) rhombohedral, AFD/FE *R*3*c* ($a^-_+a^-_+a^-_+$) rhombohedral and AFD/AFE *Pbam* orthorhombic in PZO. Their volume (Å^3/f.u.) are respectively: 69.71, 72.03, 72.34, 70.89 and 70.60. In *R*3*c* phase, the cubic parameters is 4.1672 Å, the angle is 89.7°, the octahedral rotation is 5.6° and polarization in the [111] direction 66.01 μC/cm^2. The energies were calculated with the two functional GGA-WC and LDA. The energy in GGA-WC consist here two calculations, the first calculation (cal. 1), was actually completely relaxing the cell, and the second (cal. 2) has been made keeping the cubic volume, i.e. without relaxation of the strain.

calculations give an opposite trend; it is rather the AFD *Pnma* phase ($a^-b^+a^-$) which is the lowest energy followed by AP *Pbam*−*II* phase and above, finally the FE *R*3*m* phase (AFD, −285 meV/f.u.; AP, −252 meV/f.u. and FE, −143 meV/f.u.). The AFD *Imma* is found lower in energy (−285 meV/f.u.) than AP *Pbam*−*II* phase. Let's finally analyze the behavior of PZO when allowing the couplings of all these modes we just studied individually.

8 The distorted phases

Consequently of the analysis of the condensation mode by mode of instabilities observed in the PZO cubic phase, in order to identify the lowest energy phase we relaxed, in addition to the known *Pbam* phase, non-centrosymmetric *R*3*c* ($a^-_+a^-_+a^-_+$) phase, which combines the antiphase rotations (R^+_4 mode) and ferroelectricity (Γ^-_4 mode) in three directions. In Fig. 10 we present the volumes and energy gains of PZO main phases.

Looking at the Fig. 10, the two approximations, GGA-WC and LDA, give two different tendencies between *R*3*c* and *Pbam*. In GGA-WC, it's the *R*3*c* which is more stable than the *Pbam* phase ($-260 < -254$ meV/f.u.), but the LDA, as reported in the literature [28], reveal an opposite tendency, stabilizing *Pbam* lower than *R*3*c* ($-323 < -316$ meV/f.u.). Anyway, the two approximations show the energetical proximity exiting between the two phases as is required in an AFE compound. For *R*3*c* phase, we have not found nor any experimental data or theoretical for comparison. We note, however, when the polar mode Γ^-_4 couple with AFD mode in *R*3*c* phase ($a^-_+a^-_+a^-_+$), this has the effect of reducing: 1° the amplitude of the spontaneous polarization (*R*3*m*, $P_s = 75$ μC/cm^2 and *R*3*c*, $P_s = 66$ μC/cm^2) and also, 2° the amplitude of rotation of oxygen octahedra ($R\bar{3}c$, $a^- = 7.0°$ and *R*3*c*, $a^- = 5.6°$). Accordingly, the volume is found also reduced. Based on analyzes in Section 4, we suggest the strong tendency of PZO to make the two phases *Pbam* (AFD/AFE) and *R*3*c* (AFD/FE) coexist at low temperatures. This behavior should characterises all the perovskite AFE compounds. The strong tendency of $PbZrO_3$ to adopt a *R*3*c* phase allows to understand the existence of this FE phase *R*3*c* in the PZT phase diagram in the vicinity of PZO.

9 Conclusions

In this paper, we reported a first-principles study of the structural and vibrational properties of $PbZrO_3$. We conducted a systematic investigation of energy savings and ways of couplings in PZO through different phases, observed and unobserved. The PZO is a good insulator with a direct gap of 2.33 eV at *X* point of the Brillouin zone.

The presence of AFD modes turns out a practical way to create phases AFD/FE and AFD/AFE, for the emergence of anti-ferroelectricity. This clarifies why the known AFE compounds systematically include AFD distortions. In this context, the FE, AP and AFD instabilities are usually in competition, and the coexistence of FE, AP and AFD instabilities with high amplitude is indispensable to create mixed phases (that is to say that if an instability is too low, it will be removed entirely from the other). To support this hypothesis, we note first that the calculation of phonon dispersion curves in the PE cubic phase high symmetry of PZO shows a rich diagram instabilities. It appears then that an important potential well for the FE mode of amplitude comparable to that of AFD modes, is an essential feature. Interestingly, all these FE, AP and AFD phases are in the same energy range (−200 meV/f.u.). The FE/AFD and AP/AFD combinations in the *R*3*c* and *Pbam* phases will allow to produce more energy gain (Fig. 11).

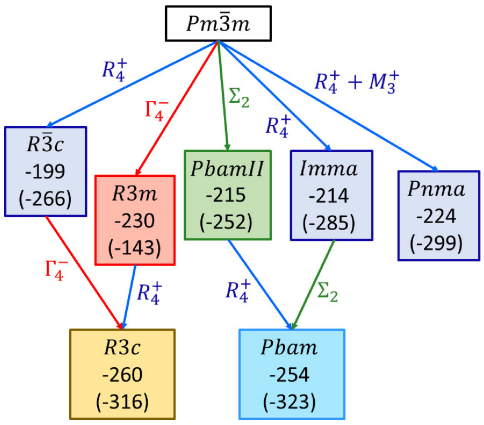

Fig. 11. (Color on line) Energy gains (meV/f.u.) of different phases in the relaxed PZO compared relative to the cubic phase (the scale is not respected, and the values in brackets are from LDA). The arrows indicate the mode type promoting the appearance of phase: blue color represent the AFD mode, green symbolise the AP mode, and the FE mode is represented by red color.

Unlike FE compounds, none of the modes individually condensed removes all others and it's their couplings which are playing a major role in the development of the ground state of lead zirconate. As summarized in Fig. 11, the coexistence of FE/AFD and AP/AFD phases nearby energy and developing separate systems tilts helps make the abrupt transition and the emergence of the antiferroelectricity as we have postulated in introduction. This is probably a second element for understanding the importance of AFD modes within AFE compounds. These various elements give a new perspective on antiferroelectricity and allow us to have a more precise idea of the origin of the AFE behavior in perovskites.

This work was supported by Belgian Technical Cooperation (BTC) and the Wallonie Bruxelles International (WBI). We used the facilities provided by the CECI supercomputing center [57]. Author thanks Prof. P. Ghosez, Doctors E. Bousquet and M. M. Schmitt both of Physique Théorique des Matériaux (ULiège) for helpful discussions.

Conflict of interest

The author declare that they have no conflict of interest.

References

1. E. Sawaguchi, H. Maniwa, and S. Hoshino, Phys. Rev. **83**, 1078 (1951) https://doi.org/10.1103/PhysRev.83.1078
2. G. Shirane, E. Sawaguchi, and Y. Takagi, Phys. Rev. **84**, 476 (1951) https://doi.org/10.1143/JPSJ.7.336
3. B. A. Scott and G. Burns, J. Am. Ceram. Soc. **55**, 331 (1972) https://doi.org/10.1111/j.1151-2916.1972.tb11303.x
4. H. Fujishita, Y. Shiozaki, N. Achiwa and E. Sawaguchi, J. Phys. Soc. Jpn. **51**, 3583 (1982) https://doi.org/10.1143/JPSJ.51.3583
5. A. M. Glazer, K. Roleder, and J. Dec, Acta Cryst. B**49**, 846 (1993) https://doi.org/10.1107/S0108768193005129
6. K. Roleder, M. Maglione, M. D. Fontana and J. Dec, J. Phys.: Condens. Matter **8**, 10669 (1996) https://doi.org/10.1088/0953-8984/8/49/051
7. N. Sicron, Y. Yacoby, E. A. Stern, and F. Dogan, J. Phys. IV France **7**, C2-1047 (1997) https://doi.org/10.1051/jp4:19972134
8. D. L. Corker, A. M. Glazer, J. Dec, K. Roleder, and R. W. Whatmore, Acta Cryst. B**53**, 135 (1997) https://doi.org/10.1107/S0108768196012414
9. K. Roleder, I. Jankowska-Sumara, G. E. Kugel, M. Maglione, M. D. Fontana and J. Dec, Phase Transitions **71**, 287 (2000) https://doi.org/10.1080/01411590008209310
10. T. Ostapchuk *et al.*, J. Phys.: Condens. Matter **13**, 2677 (2001) https://doi.org/10.1088/0953-8984/13/11/322
11. H. Fujishita and S. Hoshino, J. Phys. Soc. Jpn. **53**, 226 (1984) https://doi.org/10.1143/JPSJ.53.226
12. V. J. Tennery, J. Am. Ceram. Soc. **49**, 483 (1966) https://doi.org/10.1111/j.1151-2916.1966.tb13304.x
13. H. Fujishita, J. Phys. Soc. Jpn. **61**, 3606 (1992) https://doi.org/10.1143/JPSJ.61.3606
14. H. Fujishita and S. Katano, J. Phys. Soc. Jpn. **66**, 3484 (1997) https://doi.org/10.1143/JPSJ.66.3484
15. D. J. Singh, Phys. Rev. B **52**, 12559 (1995) https://doi.org/10.1103/PhysRevB.52.12559
16. U. V. Waghmare and K. M. Rabe, Ferroelectrics **194**, 135 (1997) https://doi.org/10.1080/00150199708016088
17. J. Baedi, S. M. Hosseini, A. Kompany, and E. Attaran Kakhki, Phys. Stat. Sol. B **245**, 2572 (2008) https://doi.org/10.1002/pssb.200743493
18. G. Pilania, D. Q. Tan, Y. Cao, V. S. Venkataramani, Q. Chen, and R. Ramprasad, J Mater Sci **44**, 5249 (2009) https://doi.org/10.1007/s10853-009-3465-0

19. D. J. Singh, Ferroelectrics **194**, 299 (1997) https://doi.org/10.1080/00150199708016101
20. S. Teslic and T. Egami, Acta Cryst. B**54**, 750 (1998) https://doi.org/10.1107/S0108768198003802
21. F. Jona, G. Shirane, F. Mazzi, and R. Pepinsky, Phys. Rev. **105**, 849 (1957) https://doi.org/10.1103/PhysRev.105.849
22. G. A. Samara, Phys. Rev. B **1**, 3777 (1970) https://doi.org/10.1103/PhysRevB.1.3777
23. X. Dai, J.-F. Li, and D. Viehland, Phys. Rev. B **51**, 2651 (1995) https://doi.org/10.1103/PhysRevB.51.2651
24. H. Liu and B. Dkhil, Zeit. Kristallogr. **226**, 163 (2011) https://doi.org/10.1524/zkri.2011.1336
25. A. M. Glazer, Acta Cryst. B **28**, 3384 (1972) https://doi.org/10.1107/S0567740872007976
26. A. M. Glazer, Acta Cryst. A**31**, 756 (1975) https://doi.org/10.1107/S0567739475001635
27. P. M. Woodward, Acta Cryst. B**53**, 44 (1977) https://doi.org/10.1107/S0108768196012050
28. B. Xu, O. Hellman, and L. Bellaiche, Phys. Rev. B **100**, 020102(R) (2019) https://doi.org/10.1103/PhysRevB.100.020102
29. J. Íñiguez, M. Stengel, S. Prosandeev, and L. Bellaiche, Phys. Rev. B **90**, 220103(R) (2014) https://doi.org/10.1103/PhysRevB.90.220103
30. R. Kagimura and D. J. Singh, Phys. Rev. B **77**, 104113 (2008) https://doi.org/10.1103/PhysRevB.77.104113
31. J. Hlinka *et al.*, Phys. Rev. Lett. **112**, 197601 (2014) https://doi.org/10.1103/PhysRevLett.112.197601
32. K. M. Rabe, in *Functional Metal Oxides: New Science and Novel Applications*, ed. by S. Ogale and V. Venkateshan (Wiley, Hoboken, NJ, 2013)
33. X. Gonze *et al.*, Comput. Mat. Science **25**, 478 (2002) https://doi.org/10.1016/S0927-0256(02)00325-7 *et al.* (2005)
34. X. Gonze *et al.*, Zeit. Kristallogr. **220**, 558 (2005) https://doi.org/10.1524/zkri.220.5.558.65066
35. X. Gonze *et al.*, Computer Phys. Comm. **180**, 2582 (2009) https://doi.org/10.1016/j.cpc.2009.07.007
36. http://www.abinit.org
37. Z. Wu and R.E. Cohen, Phys. Rev. B **73**, 235116 (2006) https://doi.org/10.1103/PhysRevB.73.235116
38. http://opium.sourceforge.net/
39. X. Gonze and C. Lee, Phys. Rev. B **55**, 10355 (1997) https://doi.org/10.1103/PhysRevB.55.10355
40. H. T. Stokes, D. M. Hatch, B. J. Campbell, ISODISTORT, ISOTROPY Software Suite, iso.byu.edu. http://stokes.byu.edu/isotropy.html.
41. D. Orobengoa, C. Capillas, M.I. Aroyo, and J.M. Perez-Mato, J. Appl. Cryst. A**42**, 820-833 (2009) http://www.cryst.ehu.es/cryst/amplimodes.html.
42. B. J. Campbell, H. T. Stokes, D. E. Tanner, and D. M. Hatch, J. Appl. Cryst. **39**, 607 (2006) http://stokes.byu.edu/iso/isodistort.php.
43. R. D. King-Smith and D. Vanderbilt, Phys. Rev. B **49**, 5828 (1993) https://doi.org/10.1103/PhysRevB.49.5828
44. E. Sawaguchi, J. Phys. Soc. Jpn. **8**, 615 (1953) https://doi.org/10.1143/JPSJ.8.615
45. S. Aoyagi, Y. Kuroiwa, A. Sawada, H. Tanaka, E. Nishibori, M. Takata, M. Sakata, J. Phys. Soc. Japan **71**, 2353-2356 (2002) https://doi.org/10.1143/jpsj.71.2353
46. R. I. Eglitis and M. Rohlfing, J. Phys.: Condens. Matter **22**, 415901 (2010) https://doi.org/10.1088/0953-8984/22/41/415901
47. Yu. F. Zhukovskii, E. A. Kotomin, S. Piskunov, D. E. Ellis, Solid State Commun. **149**, 1359 (2009) https://doi.org/10.1016/j.ssc.2009.05.023
48. H. Fujishita, Y. Ishikawa, S. Tanaka, A. O Sawaguchi and S. Katano, J. Phys. Soc. Jpn. **72**, 1426 (2003) https://doi.org/10.1143/JPSJ.72.1426
49. M. D. Johannes and D. J. Singh, Phys. Rev. B **71**, 212101 (2005) https://doi.org/10.1103/PhysRevB.71.212101
50. W. Zhong, R. D. King-Smith, and D. Vanderbilt, Phys. Rev. Lett. **72**, 3618 (1994) https://doi.org/10.1103/PhysRevLett.72.3618
51. B. K. Mani, S. Lisenkov, and I. Ponomareva, Phys. Rev. B **91**, 134112 (2015) https://doi.org/10.1103/PhysRevB.91.134112
52. E. Cockayne and K. M. Rabe, J. Phys. Chem. Solids **61**, 305 (2000) https://doi.org/10.1016/S0022-3697(99)00298-X
53. P. Tolédano and D. D. Khalyavin, Phys. Rev. B **99**, 024105 (2019) https://doi.org/10.1103/PhysRevB.99.024105
54. S. Amisi, E. Bousquet, K. Katcho, and Ph. Ghosez, Phys. Rev. B **85**, 064112 (2012) https://doi.org/10.1103/PhysRevB.85.064112
55. G. A. Samara, T. Sakudo, and K. Yoshimitsu, Phys. Rev. Lett. **35**, 1767 (1975) https://doi.org/10.1103/PhysRevLett.35.1767
56. M. Ghita, M. Fornari, D. J. Singh, S. V. Halilov, Phys. Rev. B **72**, 054114 (2005) https://doi.org/10.1103/PhysRevB.72.054114
57. https://www.ulg.ac.be/cms/c_3826073/fr/nic4, http://www.ceci-hpc.be/